[UCI]I804:24011-200000241202

2011 年 2 月
碩士學位 論文

Nanotubular Surface Morphology of Femtosecond Laser Treated Ti-35Nb-xHf Alloys for Biomaterials

朝鮮大學校 大學院

齒醫生命工學科

金在雲

Nanotubular Surface Morphology of Femtosecond Laser Treated Ti-35Nb-xHf Alloys for Biomaterials

생체재료용 펨토초레이저 처리한 Ti-35Nb-xHf 합금의 나노튜브 표면 형상

2011年 2月 25日

朝鮮大學校 大學院

齒醫生命工學科

金在雲

Nanotubular Surface Morphology of Femtosecond Laser Treated Ti-35Nb-xHf Alloys for Biomaterials

指導敎授　崔 漢 喆

이 論文을 工學 碩士學位申請 論文으로 提出함

2010年　10月

朝鮮大學校 大學院

齒醫生命工學科

金 在 雲

金在雲의 碩士學位論文을 認准함

委員張	朝鮮大學校	教 授	高永茂	印
委 員	朝鮮大學校	教 授	金炳勳	印
委 員	朝鮮大學校	教 授	崔漢喆	印

2010年 11月

朝鮮大學校 大學院

CONTENTS

LIST OF TABLES

LIST OF FIGURES

국문초록

생체재료용 펨토초레이저 처리한 Ti-35Nb-xHf 합금의 나노튜브 표면 형상

김 재 운
지도교수: 최한철, 공학박사
치의생명공학과
조선대학교 대학원

티타늄 및 티타늄 합금은 비중이 낮고 다른 금속에 비해 낮은 탄성계수를 갖으며 생체적합성이 우수하여 골절된 뼈를 접합하는 본플레이트, 인공관절, 인공장기 및 치과용 임플란트 등과 같은 생체재료로 널리 쓰이고 있다. 본 논문에서는, 펨토초레이저(10^{-15} sec)와 양극산화법을 이용하여 마이크로 기공 형성된 생체용 Ti-35Nb-xHf 합금의 나노튜브 구조에 대하여 연구하였다. Ti-35Nb-xHf 삼원계 합금은 Ti-35Nb 이원계 합금을 기본으로 하여 Hf 함량을 3, 7 및 15 wt% 가 되도록 아크용해법을 이용하여 합금을 설계하였다. 제조된 합금은 1000 ℃에서 12시간동안 열처리한 후 급냉하여 3 ㎜의 디스크형태로 시편을 준비하였다. 티타늄 사파이어 매질의 펨토초 레이저를 이용하여 표면에 마이크로 기공을 형성하였으며, 1 M H_3PO_4 + 0.8 wt.% 용액에 소량의 NaF를 첨가한 전해질 용액에서 양극산화 처리하여 표면에 나노튜브를 형성하였다.

모든 시험편의 표면은 FE-SEM, EDX, OM, XRD, XPS 및 TEM 등으로 분석하였다. 표면의 전기화학적 부식 거동은 동전위 분극시험으로 분석하였고, 마이크로 기공과 나노튜브가 형성된 Ti-35Nb-xHf 합금 표면의 접촉각을 측정하여 표면 젖음성(wettability)을 평가하여 다음과 같은 결과를 얻었다.

1. Ti-35Nb-xHf 합금은 등축정 구조로 Hf 함량이 증가할수록 입자의 크기가 줄었다. X 선 회절 분석 결과 합금에서 Hf 함량이 증가할수록 더 높은 β 상 피

크를 나타내었고 α” + β상에서 β상으로 변하였다.

2. 펨토초 레이저 기공 형성 후 나노튜브 형성한 경우는 anatase 와 rutile 의 TiO_2 상을 나타내었다. 또한, XPS 분석결과, 극초단 레이저 기공 형성 후 나노튜브 형성된 Ti-35Nb-xHf 합금의 표면에서 Ti oxide, Nb oxide 및 Hf oxide 가 관찰되었다.
3. 펨토초 레이저 기공 형성한 Ti-35Nb-xHf 합금에서 규칙적인 패턴의 마이크로 기공 (지름 25 ㎛, 패턴 폭 50 ㎛)을 볼 수 있었으며, Hf 함량 증가에 따라 마이크로 기공의 크기가 증가하며 뚜렷해졌다. 양극산화 처리로 형성된 나노튜브의 지름은 약 90 nm ~ 220 nm 의 범위와 길이는 약 4 ㎛ ~ 5 ㎛ 를 보였으며, Hf 함량이 증가할수록 나노튜브의 길이는 증가하였고, 규칙적인 형태의 튜브 구조를 보였다.
4. 펨토초 레이저 표면처리 한 Ti-35Nb-xHf 합금에서의 나노튜브 형성은 펨토초 레이저 기공 내부에서는 나노튜브 처리하지 않은 기지와 유사한 성장을 보였지만, 기공 가장자리에서는 그 형상에 따라 나노튜브의 성장이 다르게 나타났다.
5. 양극 분극 곡선으로부터, 펨토초 레이저 처리 후 나노튜브 형성한 Ti-35Nb-xHf 합금은 처리하지 않은 합금 보다 낮은 부식전류와 높은 부식전류 밀도를 보였다. 그러나 펨토초 레이저 처리 후 나노튜브 형성한 경우 더욱 안정되고 넓은 부동태 구간을 보였다.
6. 접촉각 측정으로부터, 극초단 레이저 기공 형성 후 나노튜브 처리된 Ti-35Nb-xHf 합금을 열처리하였을 시 가장 우수한 젖음성을 나타내었다.

결론적으로, 펨토초 레이저를 이용하여 기공을 형성한 후 나노튜브 처리된 Ti-35Nb-xHf 합금은 마이크로 구조와 나노 구조를 동시에 형성하여 넓은 비표면적, 높은 내식성 및 우수한 생체적합성을 가짐으로써 생체재료로 응용할 수 있음을 알 수 있었다.

Ⅰ. INTRODUCTION

Titanium and its alloys, especially the Ti-6Al-4V alloy (α + β type), are the most attractive biocompatible alloys due to their excellent combination of mechanical properties, corrosion resistance, and biocompatibility [1]. However, Al and V are released from the alloy inside the body and these ions mix in the main body stream. The release of Al even small amounts of these ions may cause local irritation of the tissues surrounding the implant [2]. For improving this problem, new titanium alloys that consist of elements with low toxicity have been developed. some researchers have focus on Ti-Nb-Zr, Ti-Ta-Zr and Ti-Nb-Hf alloy system with controlling the contents of Ta, Nb, Hf and Zr elements [3, 4]. In this particular, Nb of 4d transition metallic element is one of the most effective titanium β-stabilizer. Especially, atoms of Nb occupy exclusively the Ti sites resulting in solid-solution strengthening and precipitation hardening [5]. Also, since hafnium belongs to the same group as titanium in the periodic table of elements, titanium alloyed with hafnium will likely to have good corrosion characteristics. Hafnium, as a β isomorphous element, shows complete mutual solubility in both α and β structured titanium phases, the same as Zr element, which is also beneficial for good corrosion resistance [6]. Therefore, The excellent characteristics of Nb and Hf are the forces driving the introduction of Ti-Nb-Hf alloys into the field of biomaterials. Surface properties play an important role in the osseointegration, namely the rough surface seems to promote the growth of the bone tissue around the implant [7.8]. For rough surface texturing, many studies had demonstrated the advantages of femtosecond laser pulses, including a negligible heat affected zone, precise ablation threshold, high repeatability and efficiency, highly precise control of ablation geometry and the ability to ablate sub-diffraction limited features [9]. The high degree of biocompatibility of Ti alloys is usually ascribed to their ability to form stable and dense oxide layers consisting mainly of TiO_2. The native oxide layers on Ti are usually 2 ~ 5 nm thick and are spontaneously rebuilt in most environments whenever they are mechanically damaged. It is believed that thicker and more stable TiO_2 based oxide surfaces a regenerally favorable for surface bioactivity [10,11]. A possible way to modify the surface of the titanium substrate is the formation of self-organized TiO_2 nanotube layers by anodization under specific electrochemical conditions [12].

In this paper, we investigated the effects of nanotubular surface morphology of femtosecond laser textured Ti-35Nb-xHf alloys for biomaterials.

Ⅱ. BACKGROUND

2.1. Titanium properties [13]

Titanium, occasionally referred to as the “wonder metal”, has been utilized in a growing list of specialized applications since the Kroll process made the winning of this material from ores a commercial possibility in 1936. Titanium is the ninth most common element in the earth’s crust and is recovered from TiO_2-rich deposits of rutile, ilmenite and leucoxene that are found on every continent. since the discovery of titanium in 1794, and up until Kroll’s innovative process development in 1936, there had been no practical method to recover titanium metal from these ores because of its pronounced affinity for oxygen. Morden ore extraction, beneficiation and chemical processes have since enabled the large-volume manufacturing of high-grade TiO_2, an important pigment for faints and commercial products, and of titanium metal for the production of the CP (commercially pure) titanium grades, titanium based alloys and other alloys systems. the class of implantable metallic biomaterials can be divided into for sub-groups: stainless steels, the cobalt-based alloys, titanium metals, and miscellaneous others (including tantalum, gold, dental amalgams and other specialty metals).

Principal requirements for all the biomaterials, including metallics, are presently understood to be: corrosion resistance, biocompatibility, bioadhesion (bone ingrowth), mechanical properties, availability.

2.1.1 Chemistry and structure

Titanium is an allotropic element, which means that it can exist in more than one crystallographic form. The hexagonal close-packed crystal structure (hcp), also called the alpha phase, exists at room temperature. A transformation to the body-centered cubic (bcc), or beta phase, takes place when titanium solidifies from liquid or when solid titanium is heated to temperatures above 882 ℃ (Fig. 1). These two crystal structures are the basis for naming the three generally accepted classes of titanium alloys: "alpha", "alpha-beta" and "beta".

By alloying titanium metal with other elements, either crystal structure can be selectively stabilized at room temperature, thus making it possible to manufacture stable alpha, alpha-beta and beta alloys. Fig. 2 and Fig. 3 illustrates the stabilizing preference of these various alloying addictions and how material behavior characteristics are affected. Common alloying elements used to stabilize the alpha phase include aluminum, tin and oxygen, while those used to stabilize the beta phase include niobium, molybdenum, tantalum, chromium, iron and vanadium. Many alloys combine a carefully chosen combination of the two types of elements, and these are classified as "alpha-beta" alloys.

2.1.2 Unalloyed titanium and alpha titanium alloys

Unalloyed titanium grades and alloys of titanium with alpha stabilizing elements maintain their hcp crystallographic structures at room temperature and hence are classified as alpha titanium grades. These grades exhibit good elevated temperature creep properties, are weldable, and are used in cryogenic applications since hcp phase materials do not exhibit ductile-brittle transformation. Strengthening effects in alpha alloys are achieved by solid solutioning of the alloying elements.

2.1.3 Beta titanium alloys

Most beta titanium alloys contain small amounts of alpha stabilizers which permit second phase strengthening to high levels at room to moderate temperatures. The bcc beta phase is ductile, and therefore beta titanium alloys are easily cold form-able. Beta alloys are prone to ductile-brittle transformation, and thus are not used for cryogenic applications. The major alloying elements for beta alloys - molybdenum, niobium and tantalum - are also the elements that are considered to be very biocompatible, more so than the alpha stabilizing elements like aluminum and tin.

Beta alloys may be strengthened by the solid solutioning effect of the beta stabilizer additions, but large strength increases also result from small volume (typically <5%) second phase precipitation during heat treatment. Because of attractive hot and cold workability properties, much effort has been devoted to creating specialized beta titanium alloys for specific applications. Even though the interest in, and the manufacture of, beta titanium grades is growing, the total worldwide output of titanium mill products includes only a few percent of beta titanium alloys by weight.

2.1.4 Alpha-Beta titanium alloys

Those alloys that combine the metallurgically balanced amounts of both alpha and beta stabilizers are typically used in applications where optimum levels of competing characteristics are desired. This balancing of desired properties can be: high tensile strength versus fracture toughness, good creep resistance versus low cycle fatigue, high tensile strength versus high cycle fatigue. The properties of these two-phase alpha-beta titanium alloys can be tailored by heat treating and processing to adjust the microstructure and precipitation states of the beta phase to suit the metal temperature(s) for the end use application.

Table 1. tabulates strength and ductility properties of most of the

titanium bio-materials used and being considered by manufacturers of medical devices. Although some of these alloys have undergone different heat treatments, the heat treatments listed are in common use, and rather wide ranges of strength and ductility can be achieved as shown by these data. Tensile strengths from 35 ksi (242 MPa) to 145 ksi (1000 MPa) can tailored in the alpha grades by utilizing different elements of solid solution strengthening. Beta and alpha-beta alloys are shown to exhibit strengths upwards of 170 ksi (1173 MPa). The molybdenum containing beta and alpha-beta alloys can be cold drawn and direct aged to strength levels of over 220 ksi (1518 MPa) with reasonable ductility properties.

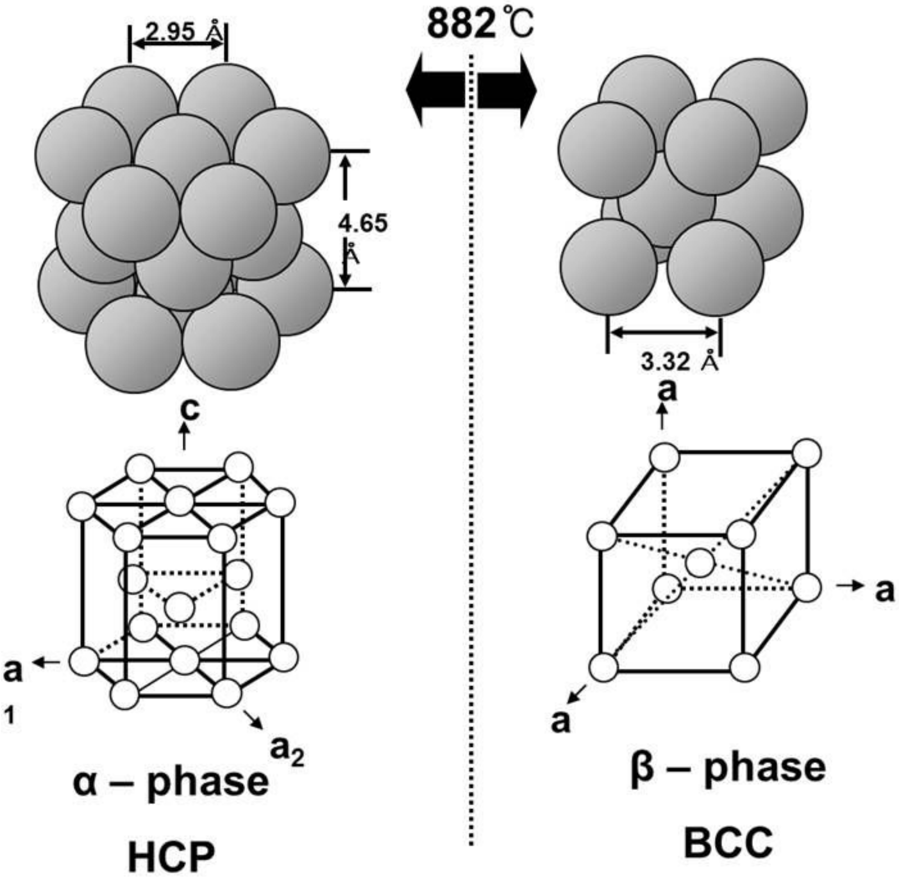

Fig. 1. Allotropic transformation of titanium [14].

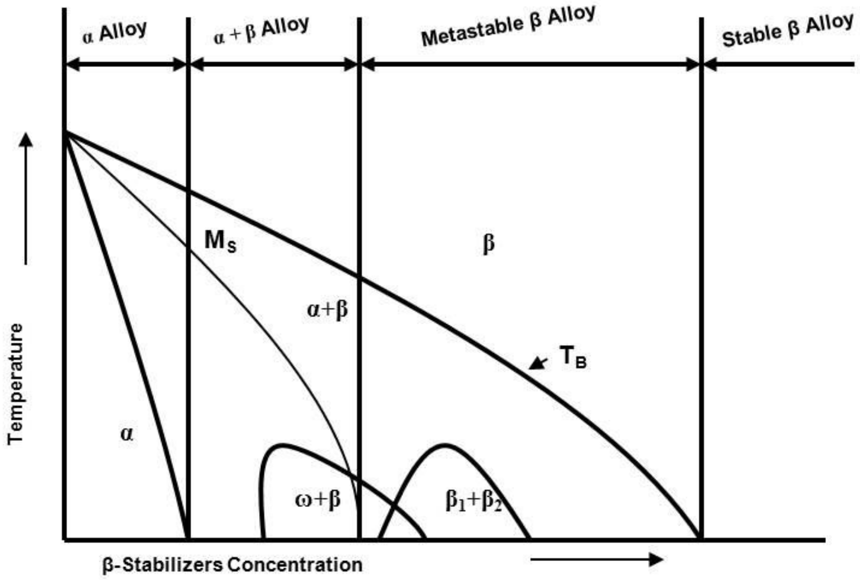

Type materials property	α and near α	α + β	β and near β
α - stabilzing element	Al, Sn, Zr, C, O, N		
β - stabilizing element			V, Mo, Nb, Ta, Cr
Type materials	Commercial pure Ti Ti−5Al−2.5Sn	Ti−6Al−4V Ti−6Al−7Nb	Ti−13Nb−13Zr Ti−30Ta

Fig. 2. Effects of alloying elements and temperature on titanium alloy structure [15].

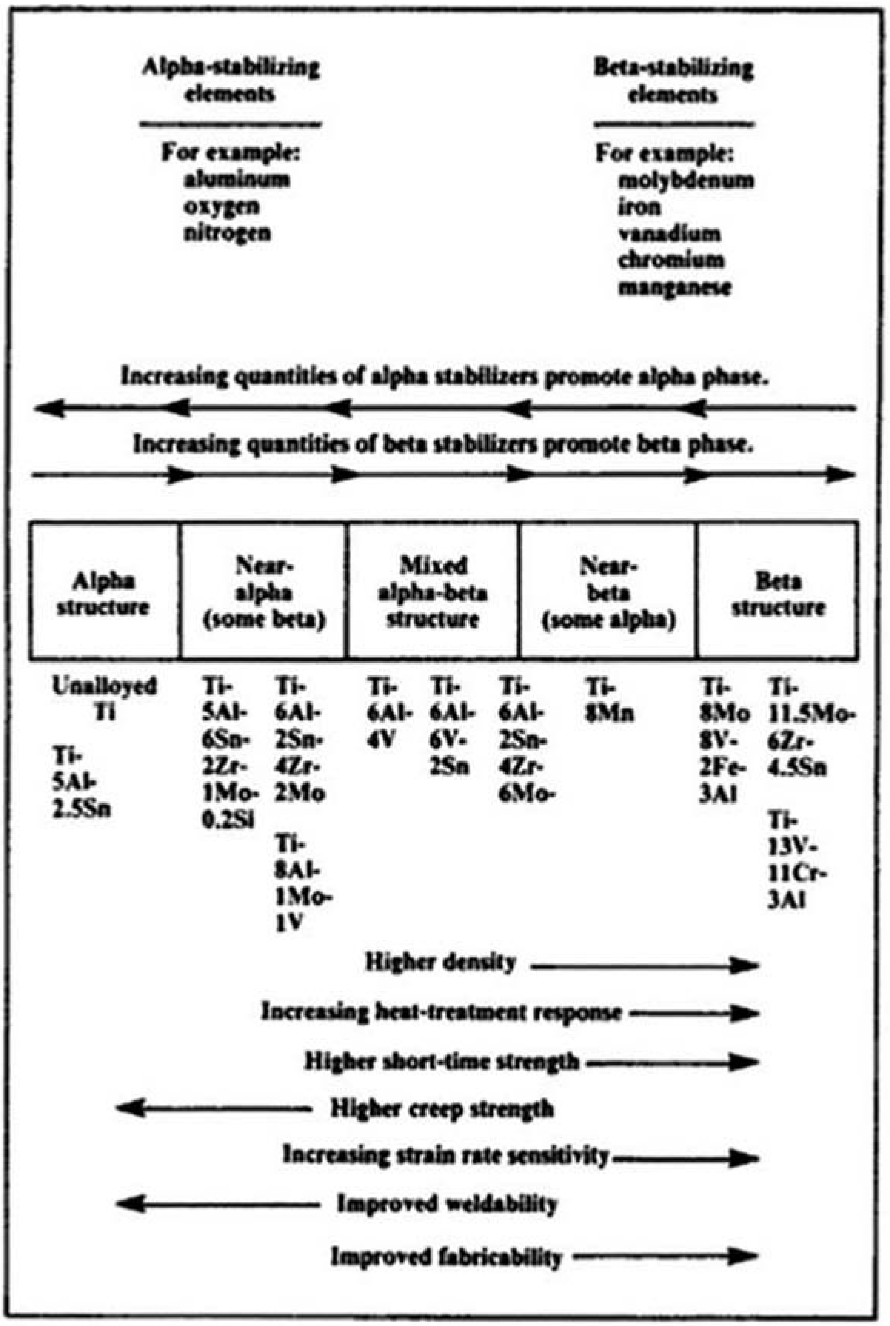

Fig. 3. Effects of alloying elements on titanium alloy structure [13].

Table 1. Mechanical properties of seleced titanium biomaterials [13]

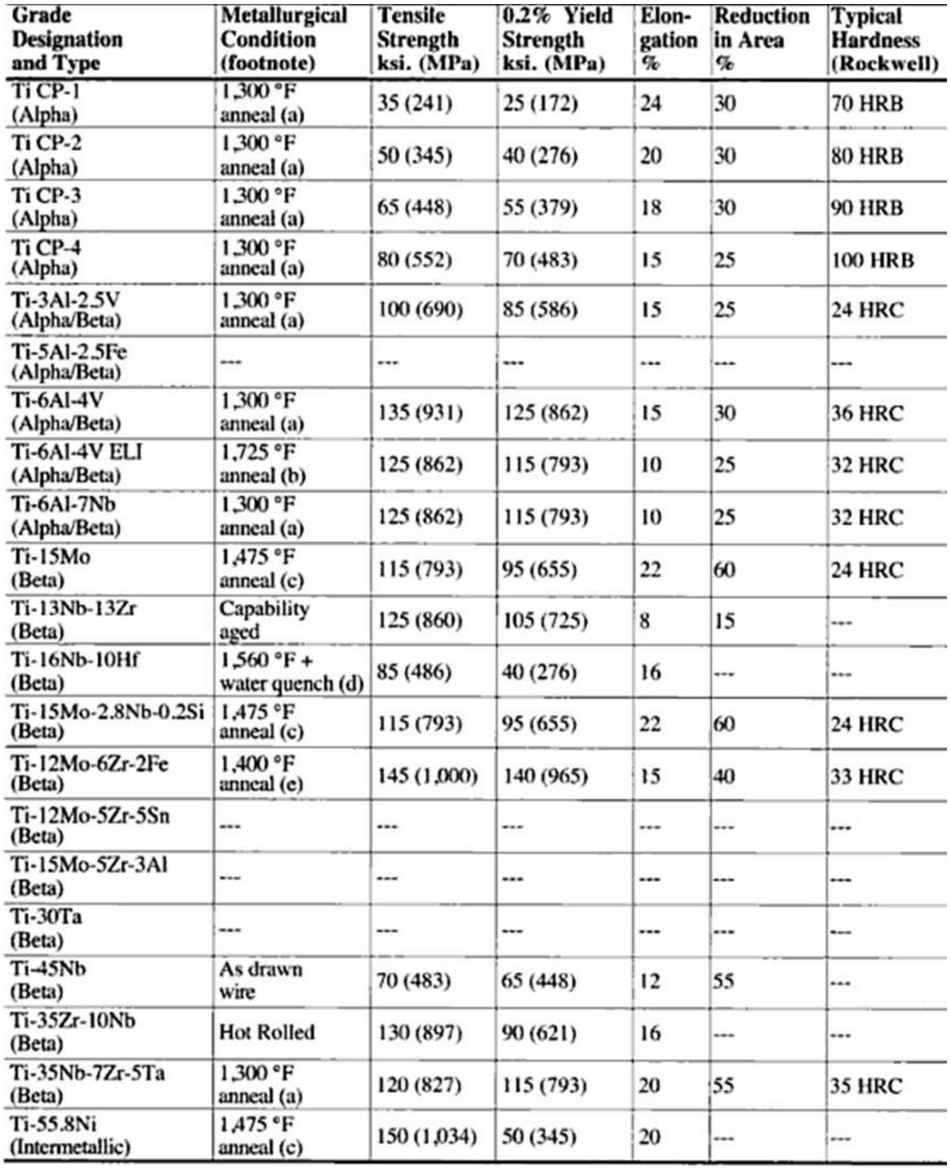

Grade Designation and Type	Metallurgical Condition (footnote)	Tensile Strength ksi. (MPa)	0.2% Yield Strength ksi. (MPa)	Elongation %	Reduction in Area %	Typical Hardness (Rockwell)
Ti CP-1 (Alpha)	1,300 °F anneal (a)	35 (241)	25 (172)	24	30	70 HRB
Ti CP-2 (Alpha)	1,300 °F anneal (a)	50 (345)	40 (276)	20	30	80 HRB
Ti CP-3 (Alpha)	1,300 °F anneal (a)	65 (448)	55 (379)	18	30	90 HRB
Ti CP-4 (Alpha)	1,300 °F anneal (a)	80 (552)	70 (483)	15	25	100 HRB
Ti-3Al-2.5V (Alpha/Beta)	1,300 °F anneal (a)	100 (690)	85 (586)	15	25	24 HRC
Ti-5Al-2.5Fe (Alpha/Beta)	---	---	---	---	---	---
Ti-6Al-4V (Alpha/Beta)	1,300 °F anneal (a)	135 (931)	125 (862)	15	30	36 HRC
Ti-6Al-4V ELI (Alpha/Beta)	1,725 °F anneal (b)	125 (862)	115 (793)	10	25	32 HRC
Ti-6Al-7Nb (Alpha/Beta)	1,300 °F anneal (a)	125 (862)	115 (793)	10	25	32 HRC
Ti-15Mo (Beta)	1,475 °F anneal (c)	115 (793)	95 (655)	22	60	24 HRC
Ti-13Nb-13Zr (Beta)	Capability aged	125 (860)	105 (725)	8	15	---
Ti-16Nb-10Hf (Beta)	1,560 °F + water quench (d)	85 (486)	40 (276)	16	---	---
Ti-15Mo-2.8Nb-0.2Si (Beta)	1,475 °F anneal (c)	115 (793)	95 (655)	22	60	24 HRC
Ti-12Mo-6Zr-2Fe (Beta)	1,400 °F anneal (e)	145 (1,000)	140 (965)	15	40	33 HRC
Ti-12Mo-5Zr-5Sn (Beta)	---	---	---	---	---	---
Ti-15Mo-5Zr-3Al (Beta)	---	---	---	---	---	---
Ti-30Ta (Beta)	---	---	---	---	---	---
Ti-45Nb (Beta)	As drawn wire	70 (483)	65 (448)	12	55	---
Ti-35Zr-10Nb (Beta)	Hot Rolled	130 (897)	90 (621)	16	---	---
Ti-35Nb-7Zr-5Ta (Beta)	1,300 °F anneal (a)	120 (827)	115 (793)	20	55	35 HRC
Ti-55.8Ni (Intermetallic)	1,475 °F anneal (c)	150 (1,034)	50 (345)	20	---	---

2.2 Titanium as a biomaterial [13]

The earliest of titanium as a material for medical, surgical and dental devices were based on the post-World War-II advances in titanium manufacturing processes for aerospace and military requirements. Thus, the earliest titanium bio-materials were commercial aerospace “hand-me-downs” because the volume requirements represented by that industry, as it grew throughout the early 1960’s, overwhelmed all other research and industrial applications for titanium combined. The four CP titanium grades (ASTM F 67), Ti-6Al-4V ELI(ASTM F 136), and “standard” Ti-6Al-4V (ASTM F 1472) were the first titanium biomaterials introduced in implantable components and devices.

The issues of corrosion resistance and biocompatibility for those titanium grades were studied and documented, and interest was generated in new “non-aerospace” titanium grades that were more suitable to the needs of the manufacturers of medical, surgical and dental devices. As device manufacturers investigated the potential advantages of titanium, new devices and improved versions of older devices were created that utilized the properties of titanium. This stimulated the need for better understanding of existing titanium formulations, and initiated research into improved titanium biomaterials more suited to the specific needs of dental applications, total joint replacement systems, medical fasteners and fracture fixation devices. In that case, the elements, which are judged to be non-toxic and non-allergic through the reported data of cell viability for pure metals, polarization resistance (corrosion resistance) and tissue compatibility of pure metals and representative metallic biomaterials, and allergic properties of pure metals, are selected as alloying elements for titanium. As a result, Nb, Ta and Hf are selected as the safest alloying elements to titanium. In addition to these elements, Mo and Sn are also selected as safer elements for living body.

2.3. Surface modification by femtosecond laser [16]

Laser manufacturing has evolved rapidly since the development of the laser in the 1960s. Laser based manufacturing technologies, such as welding, cutting, and drilling, appeared in the early history of the laser and have been actively applied to operations in various fields such as surgical operations and the restoration of cultural assets. The benefit of employing lasers in such various fields is that a laser, through a contactless method, can machine material of small size without any damage in a short time by rapidly irradiating a great deal of energy into a narrow area. Therefore, precise micromachining is possible with high peak power and short pulse duration. Because the sizes of devices today are becoming much smaller with technological advances, laser machining with ultrashort pulses has considerable meaning as a strong tool for micro-devices. Consequently, numerous researchers have studied micro-manufacturing technology using ultrashort pulse lasers. Ultrashort pulse laser micromachining technologies are being developed as a universal tool to approach micromachining from a micrometer to sub-micrometer range with flexibility and high precision. But theoretical analysis of ablation by ultrashort pulse has yet to be completed. For an ultrashort pulse duration regime, it is well known that non-thermal photochemical ablation is dominant, because laser pulse duration is shorter than the electron-lattice interaction time constant. This is a key aspect for non-thermal fabrication of micro-devices. Various industrial applications have been demonstrated by using Ti: sapphire pulse with sub-ps duration, such as fuel injection nozzles, mask repair, and optical device fabrication. More recently, however, laser-ablated micro-grooves have been used to modify the surface characteristics of biomaterials and influence cellular behavior. Unlike blast-textured surfaces that give rise to random cell orientations, laser micro-grooved implant surfaces have been shown to promote contact guidance (cell alignment), a phenomenon that involves the alignment and migration of cells along micro-grooves. This has been shown to reduce the extent of scar tissue formation and promote osseointegration. Although enhanced cell attachment and obvious cell alignment have been observed on laser-ablated micro-grooved surface after a few days culture, the actual mechanism of contact guidance and cell adhesion enhancement on laser grooves remains unclear. Therefore, There is a need to develop a fundamental understanding of the mechanisms of cell spreading and adhesion that are associated with contact guidance. These will be explored in this paper using laser micro grooved geometries with well controlled groove spacings and surface textures, since prior work has shown that both groove spacing and groove surface texture are important factors that affect the spreading and attachment of cells onto grooved implant surfaces.

2.4. Nanotube formation on the Ti alloy [17]

TiO_2 nanotubes have intrinsic properties, which include high surface area, unique physical properties, morphology, photocatalytic ability, and their inherent size and hollow geometry. These can make them extremely attractive as advanced energy storage materials with nano sized structure.

2.4.1 Fabrication of TiO_2 nanotubes by anodizing

In 1991, Zwilling et al. reported the porous surface of titania films electrochemically formed in fluorinated electrolyte by titanium anodization. A decade later Crimes et al. first reported formation of uniform titania nanotubes arrays via anodic oxidation of titanium in an hydrofluoric (HF) electrolyte. Anodization of titanium foils and thin films are conducted using a two electrode electrochemical cell with a platinum foil as cathode at a constant potential. Electrolyte composition plays a critical, and as of yet essentially unexplored role in determining the resultant nanotubes array and its chemical composition. Electrolyte composition and its pH determine the rate of nanotube array formation, as well as the rate at which the resultant oxide is dissolved. In all cases, a fluoride ion containing electrolyte is needed for nanotube array formation. Ordered nanotubular/nanoporous structures of TiO_2 or other transition metal oxides can be formed as schematically shown in Fig. 4 [18]. The key processes responsible for anodic formation of nanoporous alumina and titania appear to be the same, and are fundamental to the formation of straight titania nanotubes. The key processes are: (1) Oxide growth at the surface of the metal occurs due to interaction of the metal with O^{2-} of OH^- ions. After the formation of an initial oxide layer, these anions migrate through the oxide layer reaching the metal/oxide interface where they react with the metal. (2) Metal ions (Ti^{4+}) migration from the metal at the metal/oxide interface. Ti^{4+} cations will be ejected from the metal/oxide interface under application of an electric field that move towards the oxide/electrolyte interface. (3) Field assisted dissolution of the oxide at the oxide/electrolyte interface. Due to the applied electric field the Ti-O bond undergoes polarization and is weakened promotion dissolution of the metal cations. Ti^{4+} cations dissolve into the electrolyte, and the free O^{2-} anions migrate towards the metal/oxide interface, see process (1), to interact with the metal. (4) Chemical dissolution of the metal, or oxide, by the acidic electrolyte also takes place during anodization.

As the anodization process from the initial oxide layer, formed due to interaction of the surface Ti^{4+} ions with oxygen ions (O^{2-}) in the electrolyte, is seem uniformly across the surface. The overall reactions for anodic oxidation of titanium can be represented as

$$2H_2O \rightarrow O_2 + 4e + 4H^+ \quad (I-1)$$

$$Ti + O_2 \rightarrow TiO_2 \quad (I-2)$$

$$TiO_2 + 6F^- + 4H^+ \rightarrow TiF_6^{2-} + 2H_2O \quad (I-3)$$

In the initial stages of the anodization process field assisted dissolution dominates chemical dissolution due to the relatively large electric field across the thin oxide layer. Small pits formed due to the localize dissolution of the oxide, represented by the reaction (I-3), act as pore forming centers. Then, these pits convert into bigger pores and the pore density increases. After that, the pores spread uniformly over the surface. The pore growth occurs due to the inward movement of the oxide layer at the pore bottom (barrier layer) due to processes (I-3). The Ti^{4+} ions migrating from the metal to the oxide/electrolyte interface dissolve in the fluoride electrolyte. The rate of oxide growth at the metal/oxide interface and the rate of oxide dissolution at the pore-bottom/electrolyte interface ultimately become equal, thereafter the thickness of the barrier layer remains unchanged although it moves further into the metal making the pore deeper. The formation of small pits in the inter-pore regions which eventually leads to pore separation and tube formation. The thickness of the tubular structure ceases to increase when the chemical dissolution rate of the oxide at the mouth of the tube (top surface) becomes equal to the rate of inward movement of the metal/oxide boundary at the base of the tube. Higher anodization voltages increase the oxidation and field-assisted dissolution hence a greater nanotube layer thickness can be achieved before equilibrating with the chemical dissolution. With the onset of anodization, a thin layer of oxide forms on the titanium surface (Figure 5-a). Small pits originate in this oxide layer due to the localized dissolution of the oxide (figure 5-b) making the barrier layer at the bottom of the pits relatively thin which, in turn, increases the electric field intensity across the remaining barrier layer resulting in further pore growth (Figure 5-c). The pore entrance is not affected by electric field-assisted dissolution and hence remains relatively narrow, while the electric field distribution in the curved bottom surface of the pore causes pore widening, as well as deepening of the pore. The result is a pore with a scallop shape . As the Ti-O bond energy is high (323 kJ/mol), in the case of titania it is reasonable to assume that only pores having thin walls can be formed due to the relatively low ion mobility and relatively high chemical solubility of the oxide in the electrolyte, hence un-anodized metallic portions can initially exist between the pores. As the pores become deeper the electric field in these protruded metallic regions increases enhancing the field-assisted oxide growth and oxide dissolution, hence simultaneously with the pores well-defined inter-pore voids start forming. (Figure 5-d) Thereafter, both voids and tubes grow in equilibrium. The nanotube length increases until the electrochemical etch rate equals the chemical dissolution rate of the top independent of the anodization duration, as determined for a given electrolyte concentration and anodization potential.

This chemical dissolution, the key for the self-organized formation of the nanotube arrays, reduces the thickness for the oxide layer (barrier layer) keeping the electrochemical etching (field-assisted oxidation and dissolution) process active. No nanotubes can be formed if the chemical dissolution is too high or too low. The electrochemical etch rate depends on anodization potential as well as concentration of electrolytes. If the electrochemical etch proceeds fasten than the chemical dissolution the thickness of the barrier layer increases, which in turn reduces the electrochemical etching process to the rate determined by chemical dissolution. The chemical dissolution rate is determined by the F^- concentration and solution pH (1-3). With increasing F^- and H^+ concentrations chemical dissolution increases. Recent investigations have shown that only in a certain F^- concentration range can nanotube arrays be achieved; from 0.05 to 0.3 mol/L in acidic solution. The anodic potential at which nanobutes are formed is related to the F^- concentration, with higher potentials requiring electrolytes of higher F^- concentration.

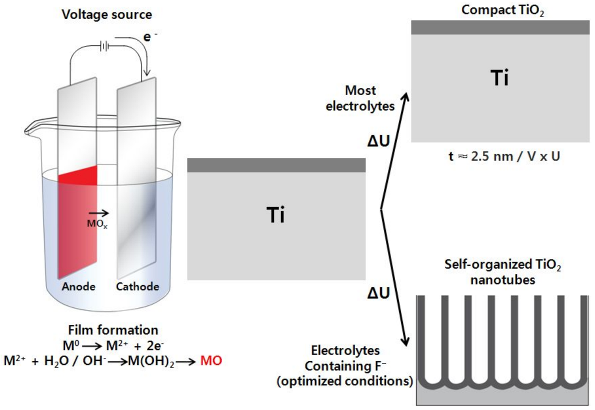

Fig. 4. Schematic set up for anodizing experiments [18].

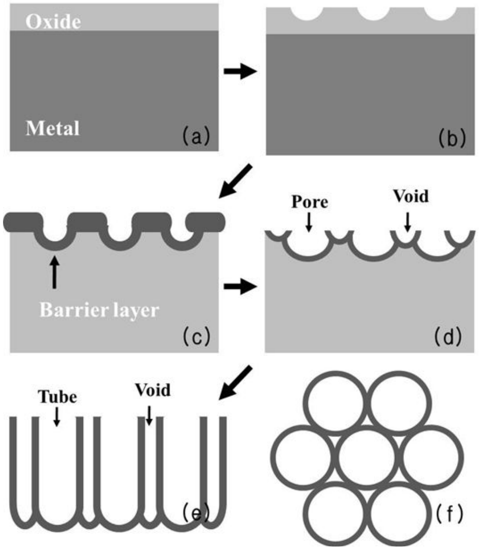

Fig. 5. Schematic diagram of the nanotube growth [17].

III. MATERIALS AND METHODS

3.1. Preparation of Ti-35Nb-xHf alloys

The Ti-35Nb-xHf alloys, with Hf contents ranging from 3, 7 and 15 wt.% were prepared using CP titanium (G&S Titanium, Grade 4, USA), Niobium and Hafnium (Kurt J. Lesker Company, 99.95 wt.% purity, USA). All materials were cleaned by ultrasonic cleaner in acetone, and dried in blowing air.

The Ti-35Nb-xHf alloys were manufactured from the component metals, using a vacuum arc-melting furnace (SVT, KOREA) with a water-cooled copper hearth and a high-purity Ar atmosphere. Sponge Ti was initially melted in the chamber to serve as an oxygen scavenger to minimize the residual oxygen level before melting the prepared alloy. The Ti-35Nb-xHf ingots were remelted at least six times in order to avoid inhomogeneity. The ingots of Ti-35Nb-xHf alloy were obtained in the form of rod with about length of 60 mm and diameter of 10 mm, and ingots were approximately 20 g in weight. The ingots of Ti-35Nb-xHf alloy were homogenized in Ar atmosphere at 1000 ℃ (MSTF-1650, MS Eng, KOREA) for 12h followed by quenching into 0 ℃ water. For manufacture the cylindrical specimens with diameter of 10 mm and thickness of 3 mm), ingots were cut off by diamond wheel cutting system (Accutom-5, Struers, Denmark). The sliced samples were mechanically abraded with SiC and then polished to 1 ㎛ using by Al_2O_3 suspension, and then ultrasonically cleaned in acetone and distilled water and finally dried in air.

3.2. Analysis of surface characteristics for Ti-35Nb-xHf alloys

The phase and composition of the Ti-35Nb-xHf alloys and nanotube formed and femtosecond laser textured surfaces were determined by using an X-ray diffractometer (XRD, X`pert PRO, Philips). Ni-filtered Cu Kα radiation was used in this study. Phase was identified by matching each characteristic peak with JCPDS files. The Ti-35Nb-xHf alloys, nanotube surfaces and femtosecond laser textured surface were observed by optical microscopy (OM, oympus, BX 60M, Japan), field-emission scanning electron microscopy (FE-SEM, Hitachi, 4800, Japan) and energy dispersive x-ray analysis (EDX, Oxford ISIS 310, England). The etching treatment was performed in Keller's reagent with 2 ml HF, 3 ml HCl, 5 ml HNO_3, 190 ml H_2O.

3.3. Femtosecond laser texturing on the alloy surface

For surface texturing, an amplified Ti: sapphire laser system was used for generating 184 femtosecond (10^{-15} sec) laser pulses with the pulse energy over 30 μJ at a 1 kHz repetition rate with a central wavelength of 785 nm. It obtained a surface with uniform holes about 25 ㎛ and pattern width about 50 ㎛ by scan speed of 60 mm/s. An attenuator to reduce the output energy of the laser composed of polarizing filters. The laser beam was focused on the Ti plate surface by a lens, installed in a processing equipment as shown in Fig. 6 [19]. The Ti-35Nb-xHf alloy's position was controlled with XYZ stages connected to a computer. Laser beam profile on the Ti-35Nb-xHf alloys was measured with a monitoring system of laser beam profile as shown in Fig. 6. Following femtosecond laser treatment, the topography of modified surface was observed using a FE-SEM.

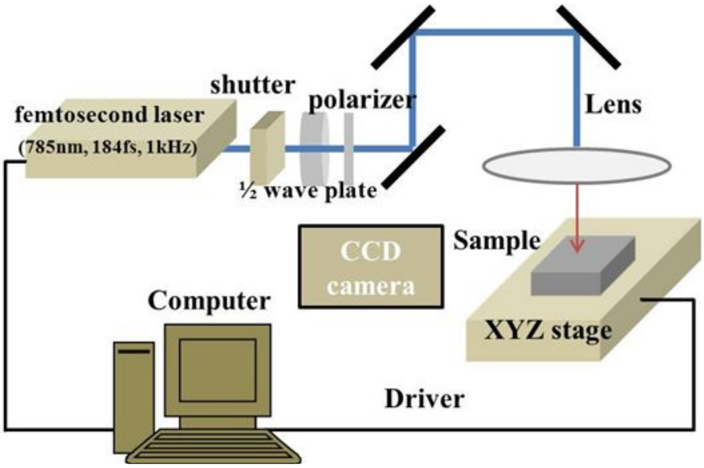

Fig. 6. Schematic diagram of femtosecond laser texturing setup [19].

3.4. Nanotube formation on the femtosecond laser textured Ti-35Nb-xHf alloys

The electrochemical experiment consisted of a three electrode configuration with platinum and saturated calomel electrode (SCE) as a counter and a reference electrode, respectively. All nanotube formation experiments were carried out at constant voltage (10 V) for 2h (potentiostat 362, EG&G Company, USA). The electrolyte was composed of 1 M H_3PO_4 + 0.8 wt.% NaF. In order to investigate the crystallinity of nanotube surface, annealing treatment was performed in Ar atmosphere at 550 ℃ for 1h and cooled in furnace.

The morphology of the porous titanium oxide was characterized by a field-emission scanning electron microscopy (FE-SEM, Hitachi S-4800, Japan) and scanning transmission electron microscope (STEM, JEM-2100F, JEOL, Japan).For precious chemical analysis of nanotube oxide surface, the samples were analyzed using a X-ray photoelectron spectroscopy (XPS, Kratos Axis Ultra DLD Multi-Technique) with Al Kα excitation. The surface of specimens was sputtered with 15 kV and 25 W Ar^+ ion beam for 2 min prior to XPS analyses to remove the surface contamination. The XPS binding energies are calibrated to give a C 1s of 280.0 eV. The binding energy of the target was O 1s, Ti 2p, Nb 3d and Hf 3d, respectively.

3.5. Corrosion test for Ti-35Nb-xHf alloys

Corrosion behaviors were investigated using a standard three-electrode cell having the specimen as a working electrode and a high dense carbon counter electrode. The potential of the working electrode was measured against a saturated calomel electrode (SCE) and all specimen potentials were referenced to this electrode. The corrosion properties of the specimens were first examined by a potentiodynamic polarization test (potential range from -1500 to 2000 mV) at scan rate of 1.67 mV/s in 0.9 % NaCl solution at 36.5 ± 1 ℃. (PARSTAT 2273, EG&G Company, USA). Using an automatic data acquisition system, the potentiodynamic polarization curves were plotted and both corrosion rate and potential were estimated by Tafel plots by using both anodic and cathodic branches. The condition of electrochemical corrosion test were shown in Table 2.

Table 2. The conditions of electrochemical corrosion test

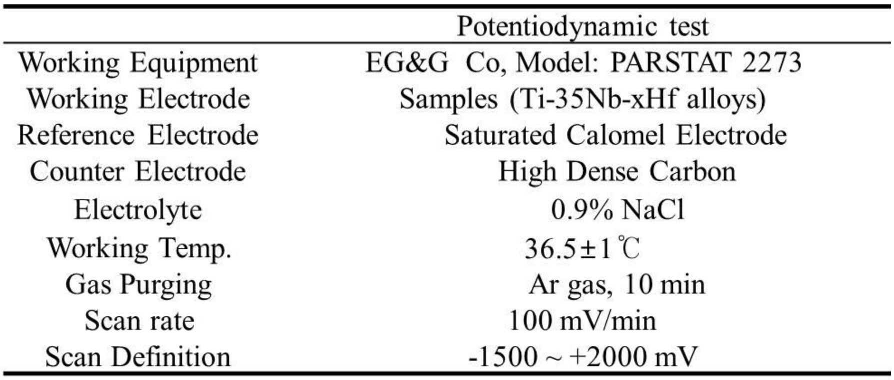

	Potentiodynamic test
Working Equipment	EG&G Co, Model: PARSTAT 2273
Working Electrode	Samples (Ti-35Nb-xHf alloys)
Reference Electrode	Saturated Calomel Electrode
Counter Electrode	High Dense Carbon
Electrolyte	0.9% NaCl
Working Temp.	36.5±1℃
Gas Purging	Ar gas, 10 min
Scan rate	100 mV/min
Scan Definition	-1500 ~ +2000 mV

3.6. Surface wettability test of nanotube formed on the femtosecond laser textured Ti-35Nb-xHf alloys

Surface wettability test was performed on the polished surface and femtosecond laser textured surface using a water contact angle goniometer (Kruss DSA100, Germany) in sessile drop mode with 5 ㎕ drops.

Ⅳ. RESULTS AND DISCUSSION

4.1. Microstructures of Ti-35Nb-xHf alloys

Fig. 7 and Fig. 8 shows the microstructures of the Ti-35Nb-xHf alloys with different Hf content (3, 7 and 15 wt.%) after heat treatment at 1000 ℃ for 12h in Ar atmosphere, followed by 0 ℃ water quenching. Microstructures of Ti-35Nb-xHf alloys were changed from α” + β phases to β phases with Hf content and all samples show the equi-axed structure, especially, Ti-35Nb-3Hf alloys shows the martensitic structure in matrix. It can be seen that the Hf increase to the Ti-35Nb alloys suppresses the precipitation of the metastable α” martensitic phase and stabilizes the β phase during the quenching process, showing the similar effect with the Zr element [20]. The grain size is smaller by increment of Hf content. Especially, Ti-35Nb-15Hf (Fig. 7c) shows the smallest grain size with consist of β phase which can play a role to improve some mechanical properties, predominantly, decrease elastic modulus of Ti-35Nb-xHf alloy. Therefore, Ti-35Nb-15Hf alloy is good for biomaterial use in the field of decreasing the stress shielding effect such as orthopedic implant and dental implant.

Fig. 9 shows the EDS results on confirmation of chemical composition of alloys. All samples show the entirely homogenized composition.

Fig. 10 shows the peaks on the XRD patterns of the homogenized Ti-35Nb-xHf alloys. The XRD peaks were identified using the JCPDS diffraction data for element standards. The peak intensity of Ti-35Nb-xHf alloys showed higher β phase with increment of Hf content, whereas, that of α” phase decreased. It is reported that the amount of α" phase increases with increasing cooling rate due to the transformation of β phase into α" phase [21]. From the results of microstructure observation and XRD analysis, which was the micro structures of Ti-35Nb-xHf alloy mainly showed β phase, which was verified very low elastic modulus and closest to bone modeling [22].

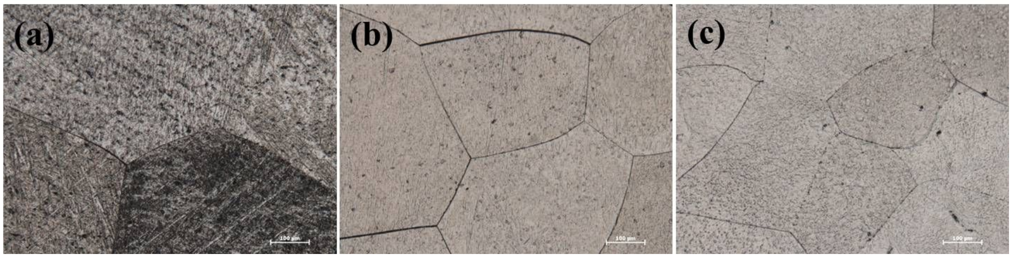

Fig. 7. OM images of Ti-35Nb-xHf alloys after heat treatment at 1000 ℃ for 12 h in Ar atmosphere, followed by 0 ℃ water quenching: (a) Ti-35Nb-3Hf, (b) Ti-35Nb-7Hf, (c) Ti-35Nb-15Hf.

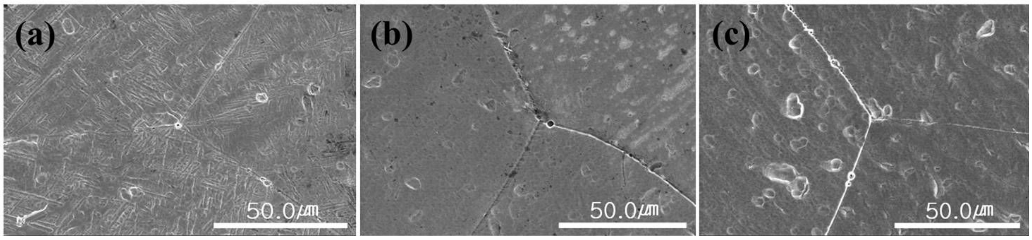

Fig. 8. FE-SEM images of Ti-35Nb-xHf alloys after heat treatment at 1000 ℃ for 12 h in Ar atmosphere, followed by 0 ℃ water quenching: (a) Ti-35Nb-3Hf, (b) Ti-35Nb-7Hf, (c) Ti-35Nb-15Hf.

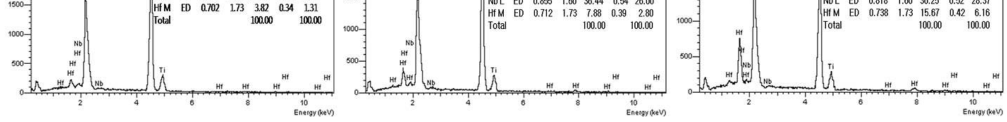

(a)

Elmt	Spect. Type	Inten. Corrn.	Std Corrn.	Element %	Sigma %	Atomic %
Ti K	ED	0.977	1.27	57.47	0.53	73.25
Nb L	ED	0.876	1.60	38.71	0.51	25.44
Hf M	ED	0.702	1.73	3.82	0.34	1.31
Total				100.00		100.00

(b)

Elmt	Spect. Type	Inten. Corrn.	Std Corrn.	Element %	Sigma %	Atomic %
Ti K	ED	0.980	1.27	55.68	0.54	71.20
Nb L	ED	0.855	1.60	36.44	0.54	26.00
Hf M	ED	0.712	1.73	7.88	0.39	2.80
Total				100.00		100.00

(c)

Elmt	Spect. Type	Inten. Corrn.	Std Corrn.	Element %	Sigma %	Atomic %
Ti K	ED	0.988	1.27	48.08	0.49	65.47
Nb L	ED	0.818	1.60	36.25	0.52	28.37
Hf M	ED	0.738	1.73	15.67	0.42	6.16
Total				100.00		100.00

Fig. 9. EDS peaks of Ti-35Nb-xHf alloys after heat treatment at 1000 ℃ for 12 h in Ar atmosphere, followed by 0 ℃ water quenching: (a) Ti-35Ntb-3Hf, (b) Ti-35Nb-7Hf, (c) Ti-35Nb-15Hf.

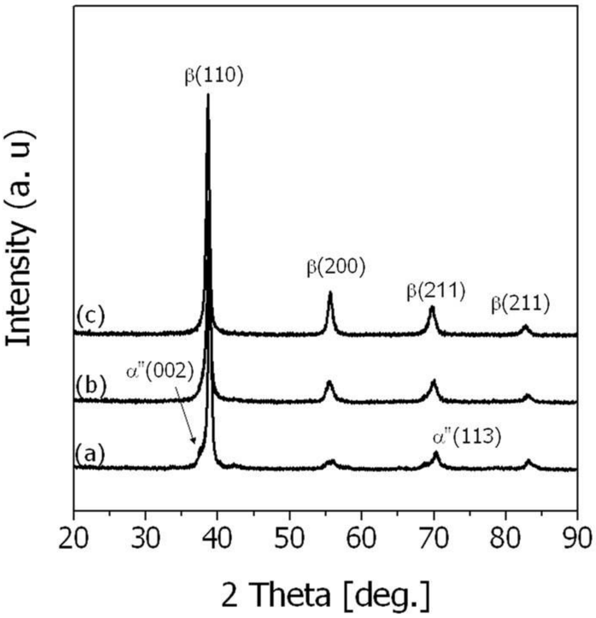

Fig. 10. XRD peaks of Ti-35Nb-xHf alloys after heat treatment at 1000 ℃ for 12 h in Ar atmosphere, followed by 0 ℃ water quenching:
(a) Ti-35Nb-3Hf, (b) Ti-35Nb-7Hf, (c) Ti-35Nb-15Hf.

4.2. Femtosecond laser textured surface of Ti-35Nb-xHf alloys

Fig. 11 show the SEM image the crater ablated by femtosecond single laser pulses irradiation. It is clear from the figure that arrays of crater (micropores) have been formed regularly on the Ti-35Nb-xHf surface. The femtosecond laser treatment is more controllable than other physical treatment methods, not only on the process parameters, but also on the size of microholes, such as plasma spraying, sand blasting and acid etching [23].

The crater diameter of Ti-35Nb-xHf alloys is about 25 ㎛ and distance from crater center to center is 50 ㎛ by scan speed of 60 mm/s. The ablation of femtosecond laser textured hole increased with increasing Hf content. It is thought that melting point of Ti-35Nb system can be changed with Hf content. That is, melting point of Ti is 1668 ℃, Hf is 2233 ℃, Nb is 2477 ℃, when the femtosecond laser was focused on specimen surface. When alloyed with Ti-35Nb, Hf plays role to gradually decrease the melting point of Ti-35Nb-xHf alloy, therefore, Ti-35Nb-15Hf shows the largest laser ablation crater on the surface.

Utilizing femtosecond laser pulses to make micro texturing surface is an attractive technique, and one of the most prominent characteristics is that precise control can be achieved by adjusting various parameters. Unlike common lasers which can only produce the holes or pores over hundreds of micrometers, femtosecond laser can create micro crater or holes about several micrometers with high precision [23] as shown in Fig. 11.

From the Fig. 11, there is an application that mechanical interlocking of bone is essential to the improved performance of endosseous implant. One possible explanation is given by the adaption of bone to mechanical loading played by the osteocytes acting as mechanosensors [24]. Evidence of the important relevance of increased bone to implant contact has been provided by measurement of the physical interaction of micron level rough implants with bone [24].

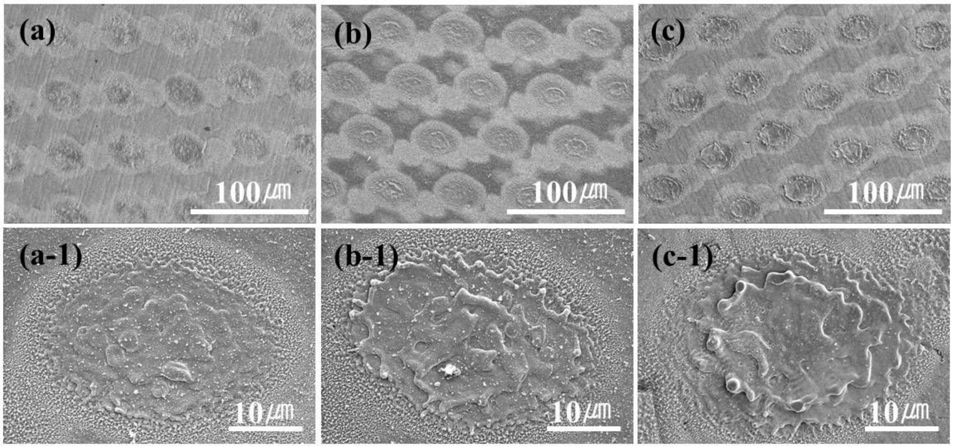

Fig. 11 SEM images of femtosecond laser textured Ti-35Nb-xHf alloys by femtosecond single laser pulses irradiation:
(a) Ti-35Nb-3Hf, (b) Ti-35Nb-7Hf, (c) Ti-35Nb-15Hf.

4.3. The nanotubular structure of Ti-35Nb-xHf alloy after femtosecond laser texturing

Fig. 12 shows SEM image the nanotube formed on femtosecond laser textured Ti-35Nb-xHf. Nanotube was formed on the arrays of micropores and on non-textured surface. The diameter of microholes of Ti-35Nb-3Hf, 7Hf and 15Hf is about 18 ㎛, 23 ㎛ and 25 ㎛, respectively, The diameter of ultrashort laser textured hole increased with Hf content. Highly regular and ordered hybrid structures (micro/nano) have been formed on the Ti-35Nb-xHf surface. In the case of nanotube formation at around the crater, irregular tube was formed due to spatter during texturing by laser.

It is different from non-laser textured samples. In the center of femtosecond laser crater, nanotube morphology was formed like a non-femtosecond laser treated sample, whereas, in the edge of femtosecond laser crater, nanotube was formed with different topography. It is thought that nanotube nucleation occur in the direction of perpendicular on oxide film surface as shown in Fig. 13.

Fig. 13(a) show images of nanotube formed on femtosecond laser textured Ti-35Nb-15Hf alloy. The nanotubes of Fig. 13(b) have an inner average diameter from about 150 nm, with a tube wall thickness of about 20 nm. Fig. 13(c) show the edge of femtosecond laser textured crater, nanotube structure was grew with different growing direction. Fig. 13(d) shows the surface of removed nanotube. The large nanotubes were surrounded by several small nanotubes from two distinctly different tube diameters at the closed bottom [25]. Fig.13(e) shows the cross-section images of the nanotube layer formed with a length of approx.5 ㎛.

Fig. 14. shows the surface morphologies, cross sectional, bottom image of nanotube formed Ti-35Nb-xHf alloys obtained by anodization in 1 M H_3PO_4 + 0.8 wt.% NaF. The tube bottom and length image was observed after mechanically flaked off from the surface after 2h of anodization. The nanotubes have a

inner average diameter from about 80 to 200 nm with a tube wall thickness of about 20 nm. It is remarkable that the pore diameter decreases with Hf concentration from 200nm in 3wt.% Hf, 160 nm in 7 wt.% Hf and 100 nm in 15 wt.% Hf. Nanotube layers inter-space increases with Hf content from 85 nm in 3 wt.% Hf, 90 nm in 7 wt.% Hf and 100 nm in 15 wt.% Hf. Nanotube layers inter-space are more and more regularly arranged as Hf content increased and changed into a more circular. The growth of TiO_2 nanotubes is a result of competition between electrochemical oxide formation and chemical dissolution of oxide by fluoride ions [26]. The nanotube layer consisted of self-organized nanotubes with the diameter of approx. 100 ~ 200 nm and a length of approx. 4.17 ~ 5.28 ㎛. The images of Fig. 14(a-2, b-2, c-2) show the bottom view of the nanotube. This bottom view was obtained from mechanically cracked sample, where some pieces of the layer were laying upside down. It is apparent that the nanotubes are open on the top while on the bottom they are closed from Fig. 14. The closed bottoms correspond to the barrier layers formation, similar to the case of porous alumina [27]. Consequently, it consists of densely packed nanotubes. Increasing the Hf content in Ti leads to much thin nanotubular layer and highly ordered layer.

Fig. 15. shows the change of nanotube size with Hf content of nanotube formed Ti-35Nb-xHf alloys. The two size-scales nanotubes consisted of large diameter and small diameter tubes. This can be ascribed to different dissolution rates of oxide layers with different alloying elementals [28]. Fig. 15(a) shows the relationship between the nanotube number and nanotube size with Hf content. Number of large tube was similar with Hf content, whereas, number of small tube increased with Hf content. Fig. 15(b) shows the relationship of pore size and tube length with Hf content increased. As the Hf content increased from 3 to 15 wt.%, the average length of the TiO_2 nanotubes was 4.17 ㎛, 4.25 ㎛, and 5.24 ㎛, respectively from Table 3. In general, diameter of nanotube was reduced. It is confirmed that Hf content

in Ti-35Nb-xHf alloy can be controlled the nanotube size for surface modification for biomaterials.

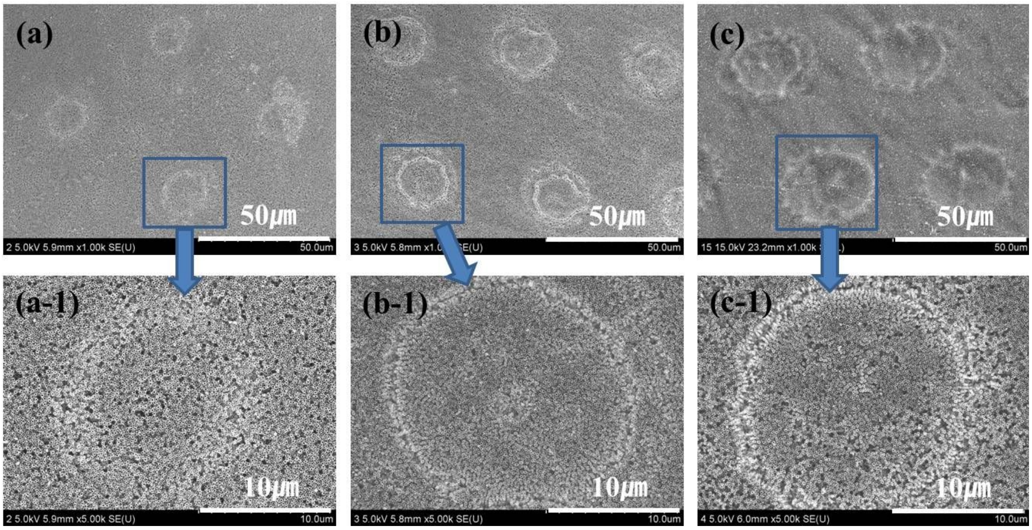

Fig. 12. The FE-SEM results of Nanotube formed on femtosecond laser textured Ti-35Nb-xHf:
(a) Ti-35Nb-3Hf, (b) Ti-35Nb-7Hf, (c) Ti-35Nb-15Hf.

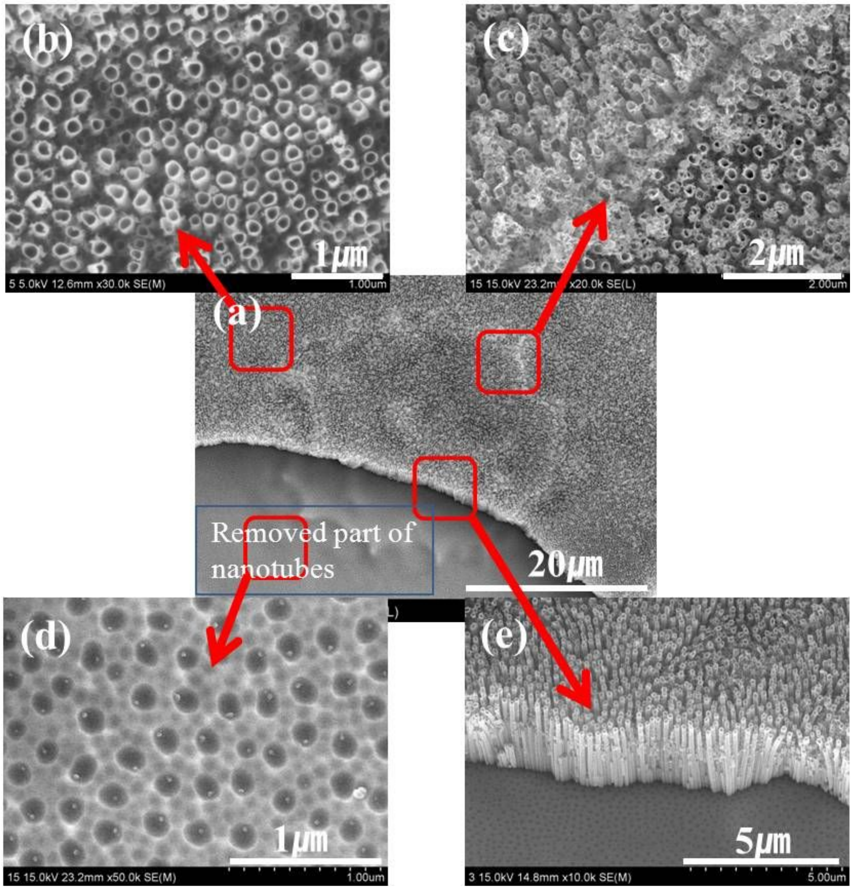

Fig. 13. The FE-SEM analysis images of a spot on surface textured Ti-35Nb-15Hf alloy.
(a) a spot of laser textured surface (b) morphology (c) edge of laser textured pore (d) bottom of removed nanotube (e) cross-section of the nanotube layer.

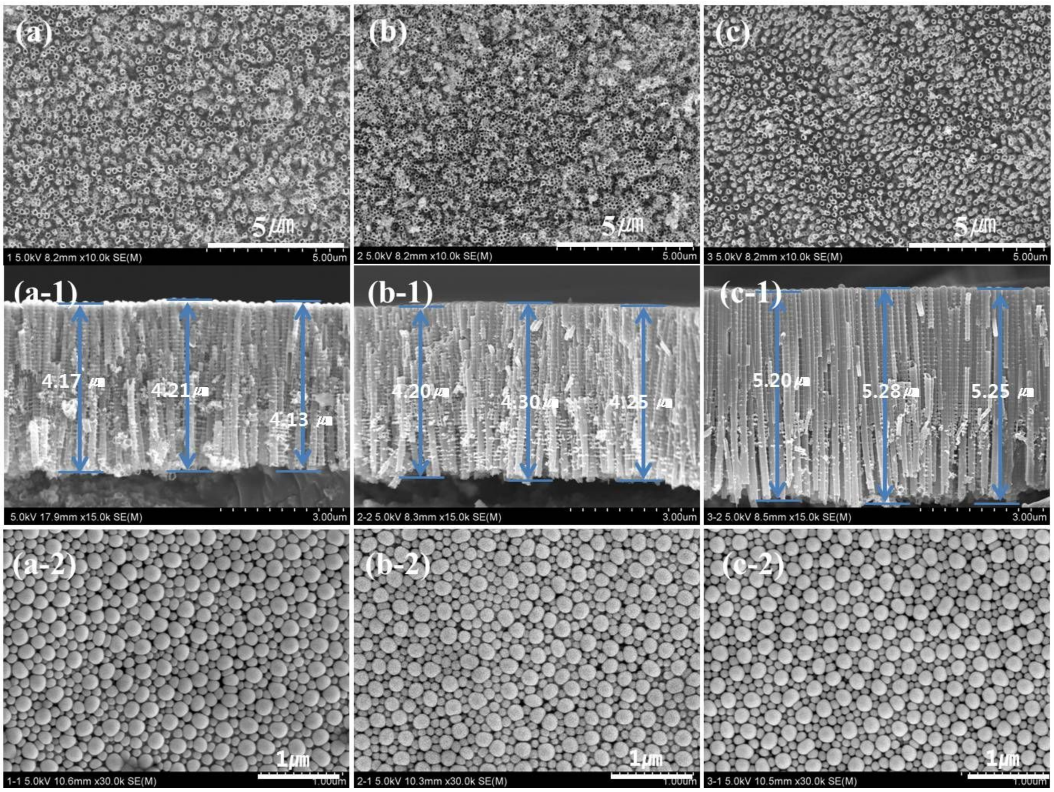

Fig. 14. FE-SEM results of the surface morphologies, cross sectional and bottom image of nanotube formed Ti-35Nb-xHf alloys.
(a) Ti-35Nb-3Hf, (b) Ti-35Nb-7Hf, (c) Ti-35Nb-15Hf.

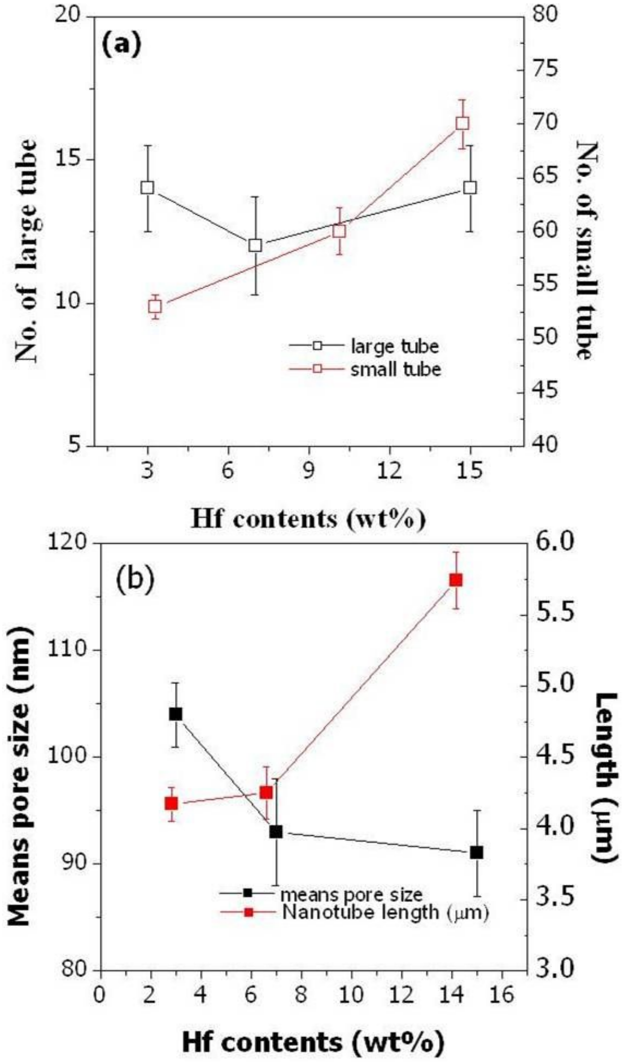

Fig. 15. The change of nanotube size with Hf content on nanotube formed Ti-35Nb-xHf alloys.

Table 3. Pore size and length of nanotube with Hf content on nanotube formed Ti-35Nb-xHf alloys

Nantube formed Ti-35Nb-xHf alloy		Ti-35Nb-3Hf	Ti-35Nb-7Hf	Ti-35Nb-15Hf
Pore size in bottom	large tube	220 nm	212 nm	190nm
	small tube	104 nm	93 nm	91 nm
length		4.17 μm	4.25 μm	5.24μm

4.4. The composition of nanotubular oxides of the femtosecond laser textured Ti-35Nb-xHf alloy

Fig. 16 shows EDS line profile an area on the Ti-35Nb-15Hf alloy covered by nanotubes and an area without nanotubes, following the formation of nanotubes in 1 M H_3PO_4 + 0.8 wt.% NaF solution. For the area covered by nanotubes, the Ti, Nb and Hf content was lower than that of the area without nanotubes, whereas the oxygen content was higher in the area with nanotubes. It can be confirmed that the nanotubes mainly consisted of alloying elements [29] as shown in Fig. 17.

Fig. 17 shows the chemical state analysis on the nanotube formed Ti-35Nb-15Hf alloy by X-ray photoelectron spectroscopy (XPS) results. The XPS binding energies of TiO, TiO_2, NbO, Nb_2O_5 and HfO_2 are about 455 eV, 459 eV,, 203 eV, 207.5 eV and 16.7 eV, respectively [30]. All spectrum variation consists of O1s, C1s, Ti2p, Nb3d and P1s on the nanotube layer. Oxide peaks exhibit higher intensity from nanotube surface, whereas, Ti, Nb and Hf peaks exhibit lower intensity from nanotube surface. Therefore, this result can be considered that nanotube formed on the femtosecond laser textured Ti-35Nb-xHf alloy surface consists of Ti, Nb and Hf oxide [29].

Fig. 18 shows the cross-sectional view images of FE-SEM, STEM and EDS of nanotube formed Ti-35Nb-15Hf alloy. FE-SEM image shows the closed nanotube bottom of Ti-35Nb-15Hf alloy. There was gradual thickening of the wall towards the bottom end of the nanotubular layers. We have carried out STEM/EDS analysis for detecting the presence of Ti, Nb and Hf oxides in the nanotubes. Barrier layer in Fig. 18(b) depended on alloying element existed in nanotube layer. Also Fig. 18(c) shows the chemical composition peaks of the three selected parts of nanotube layer. The three constituent elements of the alloy were detected in the nanotubes. Oxide peak was not detected at part 1 but it was detected at other parts. The striations were seemed to serve as an inter-connecter among the tubes and were suggested to have originated as a result of the different growth rate of nanotubes [30]. It is confirmed that length of inter-connecter in nanotube depended on Hf content and fluorine concentration due to dissolution rate of oxide film of Ti-35Nb-xHf alloy.

Fig. 19 shows XRD patterns of nanotube formed on femtosecond laser textured Ti-35Nb-xHf alloys. Nanotube structue on the femtosecond laser textured Ti-35Nb-xHf alloys are in amorphous structure. If the amorphous layers were annealed, crystallized nanotube layers can be converted to mixed structure of anatase and rutile [31]. This result indicates that the anatase and rutile phase take place at once over at 500 ℃ in oxide nanotube structure [32]. With the increasing of Hf contents, rutile peaks become more numerous and strong. But most of these phases are still composed of anatase. It is well known that anatase phase is good for the cell proliferation in bone [33]. Also, much amount of anatase phase TiO_2 are much more efficient in nucleation and growth of hydroxyapatite than only rutile phase TiO_2 presumably because of the better lattice match with hydroxyapatite phase [34].

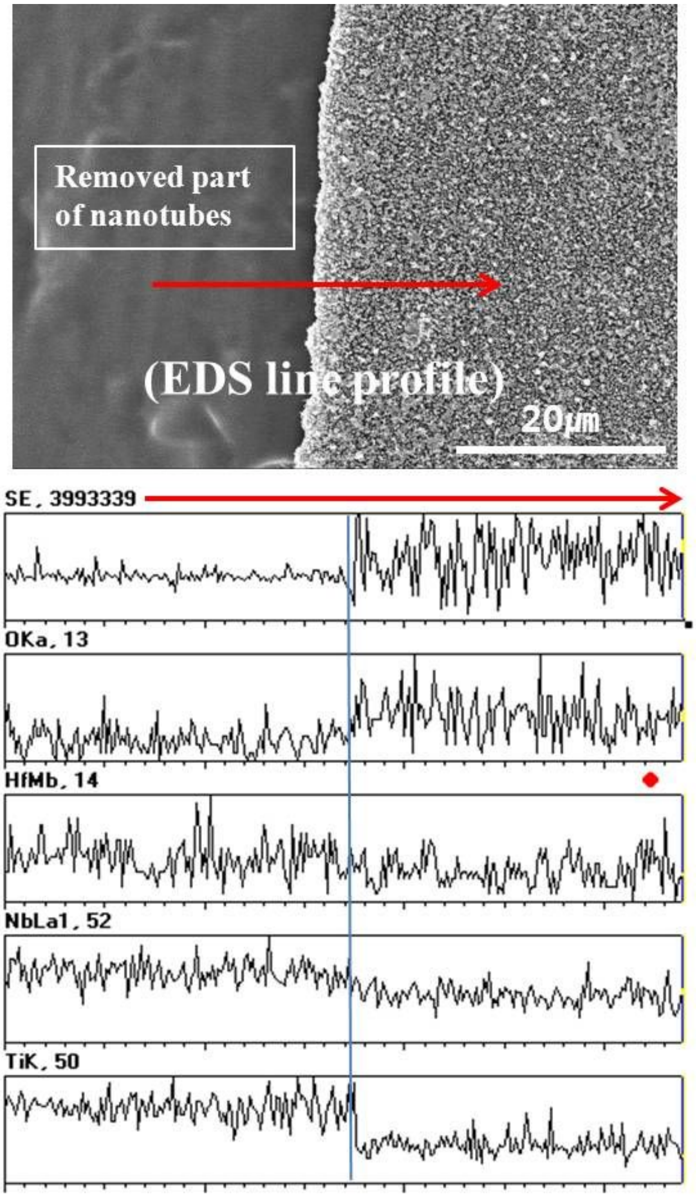

Fig.16. The EDS line profile results of nanotube formed Ti-35Nb-3Hf alloy.

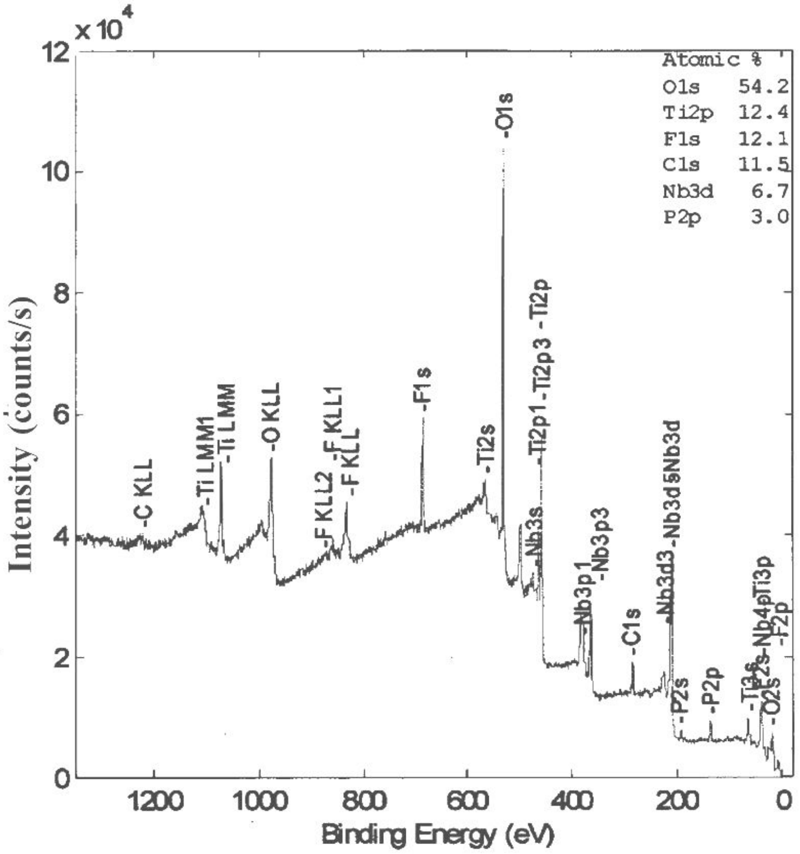

Fig. 17. XPS peaks of nanotube formed on the Ti-35Nb-15Hf alloys.

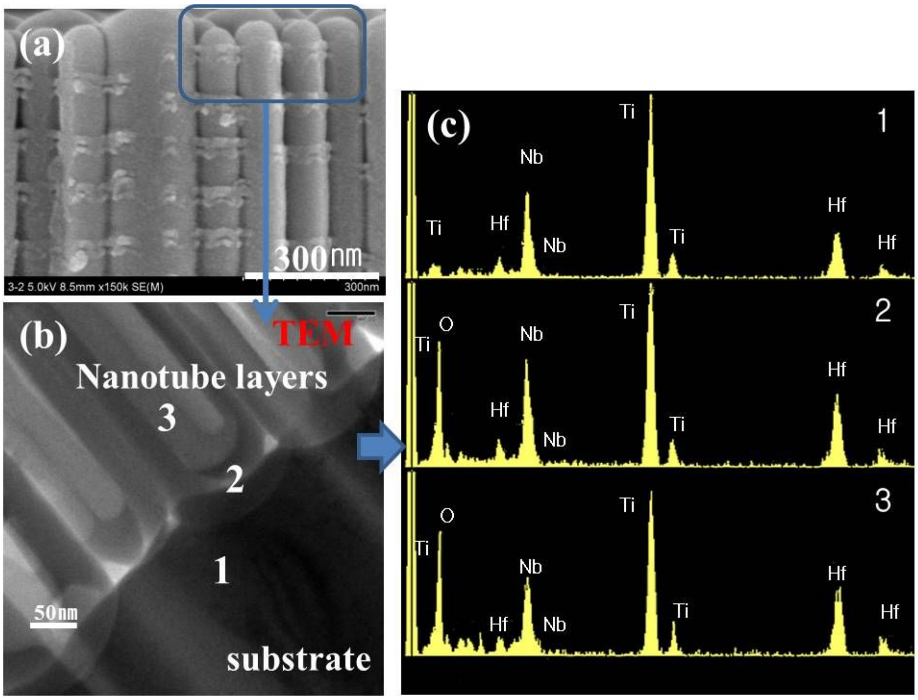

Fig. 18. FE-SEM, TEM and EDS of nanotube formed on the Ti-35Nb-15Hf alloys.

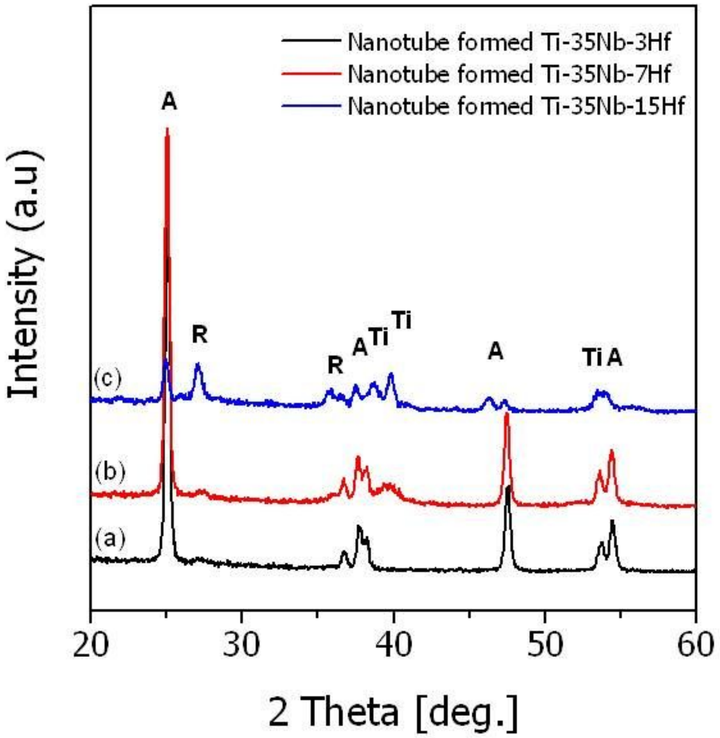

Fig. 19. XRD patterns of nanotube formed on femtosecond laser textured Ti-35Nb-xHf alloys after annealing at 500 ℃ for 1h:
(a) Ti-35Nb-3Hf, (b) Ti-35Nb-7Hf, (c) Ti-35Nb-15Hf.

4.5. Electrochemical characteristics of Ti-35Nb-xHf alloys with surface treatment

Fig. 20 shows the anodic polarization curves of water quenched Ti-35Nb-xHf alloys after potentiodynamic test in 0.9 % NaCl solution at 36.5 ± 1 ℃. The results for E_{corr} (corrosion potential), I_{corr} (corrosion current density), I_{300} (corrosion current density of oral environment at 300 mV) and I_{pp} (current density of primary passivation) from the polarization curves are given to Table 4. These values were obtained from the polarization curves and Tafel plots using both the cathodic and anodic branches of the curves, respectively. The Ti-35Nb-xHf alloys exhibit passivation region whereas, Cp-Ti and Ti-6Al-4V show the activation on the surface in 0.9 % NaCl solution. This phenomenon means the more higher corrosion resistance of Ti-35Nb-xHf alloy compare to Cp-Ti and Ti-6Al-4V. From value of Ti-35Nb-xHf alloy, E_{corr} was -570 mV ~ -420 mV, I_{corr} was 0.5 ㎂/㎠ ~ 8.0 ㎂/㎠ and I_{pp} was 7.1 ㎂/㎠ ~ 20.7 ㎂/㎠. E_{corr} and I_{corr} value were verified with Hf content in Ti-35Nb-xHf alloys. Polarization curves were shifted to left side with increasing Hf content. It is confirmed that the thick HfO_2 film is formed on the surface with addition of Hf element to Ti-35Nb system [24]. The potentiodynamic test of Ti-35Nb-xHf alloy indicated that Hf content significantly increased the electrochemical performance and it can be an important factor for the improvement of osseointegration [35].

From value of nanotube formed on the femtosecond laser textured Ti-35Nb-xHf alloy after potentiodynamic test in 0.9% NaCl solution at 36.5 ± 1 ℃. Due to large surface area of nanotube, it can be seen that E_{corr} is lower and I_{corr} is higher for the Ti-35Nb-xHf alloys with nanotube surface than those of bare surface. However, the passive region of nanotube surface is more stable and wider than bare surface, suggesting that the mixed TiO_2, Nb_2O_5 and HfO_2 film is stable [36]. Nanotube formation must be reacting with NaCl and the nanotube offer very high protection film against corrosive attack and biocompatibility between human bone and metallic implant alloy.

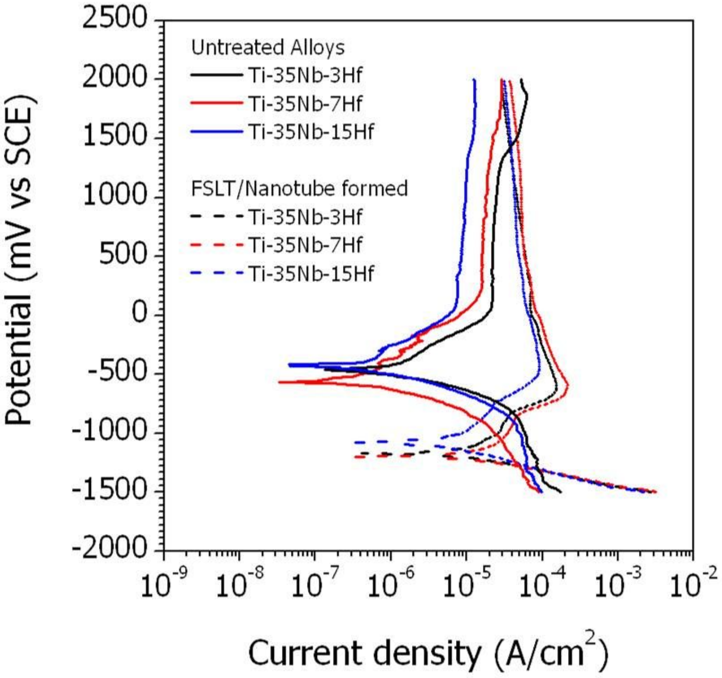

Fig. 20. Anodic polarization curves of Ti-35Nb-xHf alloys and nanotube formed on femtosecond laser textured Ti-35Nb-xHf alloys.

Table 4. Electrochemical parameter of Ti-35Nb-xHf alloys and nanotube formed on femtosecond laser textured Ti-35Nb-xHf alloys from anodic polarization curves: Corrosion current density (I_{corr}), current density at 300mV(I_{300mv}), corrosion potential (E_{corr}) and passivation current density(I_{pass})

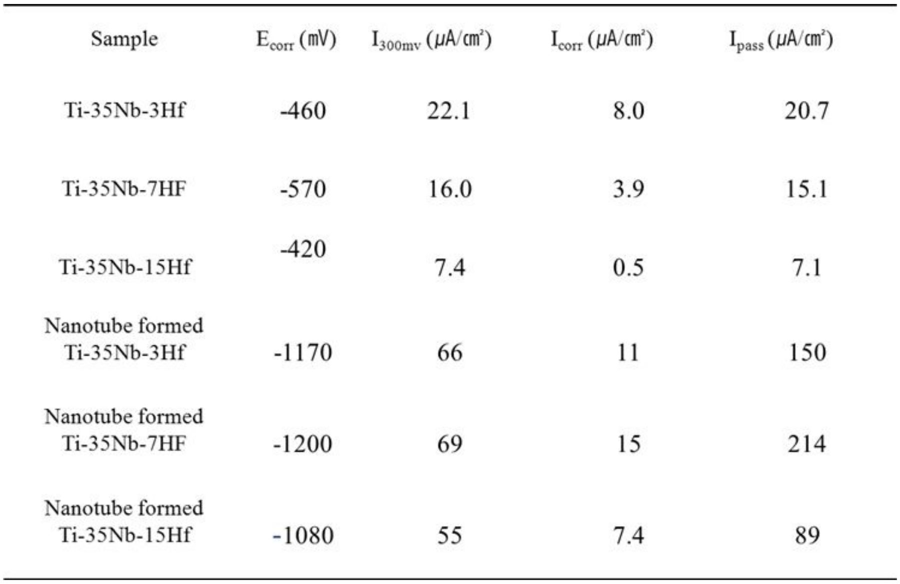

Sample	E_{corr} (mV)	I_{300mv} (μA/㎠)	I_{corr} (μA/㎠)	I_{pass} (μA/㎠)
Ti-35Nb-3Hf	-460	22.1	8.0	20.7
Ti-35Nb-7HF	-570	16.0	3.9	15.1
Ti-35Nb-15Hf	-420	7.4	0.5	7.1
Nanotube formed Ti-35Nb-3Hf	-1170	66	11	150
Nanotube formed Ti-35Nb-7HF	-1200	69	15	214
Nanotube formed Ti-35Nb-15Hf	-1080	55	7.4	89

4.6. Wettability of Ti-35Nb-xHf alloys with various surface modification

Fig. 21 shows snap shot of contact angle as an indication of surface wettability and surface biocompatibility with different surface treatment. Also, Fig. 22 shows the contact angle of water droplets measured on the different surface treatment. The values of the contact angle indicate whether the surface is hydrophilic or hydrophobic. In Fig. 21(a), the highest contact angle is average 68±2° . Fig. 21(b) show the improved the wettability and reduce the contact angle significantly (average 23±2°) due to large surface area of nanotube. Fig. 21(c) show slightly the lower value of average 21±2° compare with Fig. 21(b). Therefore, nanotube structure shows a hydrophilic behavior, whereas, Fig. 21(d) shows a super-hydrophilic behavior (average 0±2°), due to complete spreading of water on the entire and into the pores.

Osteoblasts proliferate at a faster rate on heat-treated anatase phase nanotubes compare to amorphous nanotube. The anatase phase plays an important role in proliferation and cell adhesion [33].

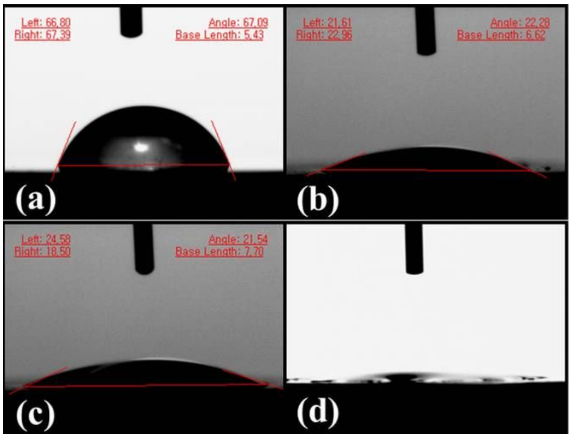

Fig. 21. Contact angle and snap shot of wettability on the surfaces: (a) Ti-35Nb-xHf alloys, (b) nanotube formed Ti-35Nb-xHf alloys, (c) nanotube formed on femtosecond laser textured Ti-35Nb-xHf alloys, (d) annealing at 500℃ for 1 h after nanotube formed on femtosecond laser textured Ti-35Nb-xHf alloys.

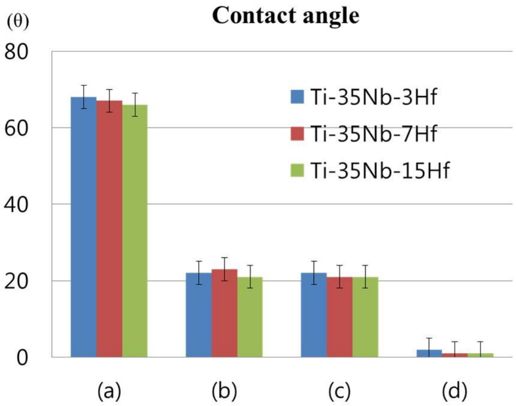

Fig. 22. Contact angle of wettability on the surfaces: (a) Ti-35Nb-xHf alloys, (b) nanotube formed Ti-35Nb-xHf alloys , (c) nanotube formed on femtosecond laser textured Ti-35Nb-xHf alloys , (d) annealing at 500℃ for 1 h after nanotube formed on femtosecond laser textured Ti-35Nb-xHf alloys.

V. CONCLUSIONS

In this study, nanotubular surface morphology of femtosecond laser textured Ti-35Nb-xHf alloys have been researched.

The results were as follows;

1. Microstructures of Ti-35Nb-xHf alloys were shown equiaxed structure and α" phase decreased, whereas β phase increased as Hf content increased.
2. Nanotube structue on the femtosecond laser textured Ti-35Nb-xHf alloys are in amorphous structure. After annealing at 500℃ for 1h, crystallized nanotube surface can be converted to mixed structure of anatase and rutile.
3. The crater diameter of Ti-35Nb-xHf alloys is about 25 ㎛ and distance from crater center to center is 50 ㎛ by scan speed of 60 mm/s. The ablation of femtosecond laser textured hole increased with increasing Hf content.
4. Nanotube formed Ti-35Nb-xHf alloys show two scale of nanotube with large (190 nm ~ 220 nm) and small (91 nm ~104 nm) diameter. The large and small nanotube structure depended on the contamination of Hf content. With increasing Hf content, Nanotube diameter of Ti-35Nb-xHf alloys decreases and nanotube length of Ti-35Nb-xHf alloys increases.
5. All spectrum variation consist of O1s, C1s, Ti2p, Nb3d and P1s on the nanotube layer. Oxide peaks exhibit higher intensity from nanotube surface than bulk surface whereas Ti, Nb and Hf peaks exhibit lower intensity from nanotube surface.
6. Polarization curves were shifted to left side with increasing Hf content . It is confirmed that the thick HfO_2 film is formed on the surface. Nanotube formed on the femtosecond laser textured Ti-35Nb-xHf alloys was shown lower E_{corr} and higher I_{corr} than those of bare surface.

However, the passive region of nanotube surface is more stable and wider than bare surface.

7. Nanotube formed on the femtosecond laser textured Ti-35Nb-xHf alloy exhibited the low contact angle and good wettability. Especially, Annealed nanotube surface shows a super-hydrophilic behavior (average 0±2°), that is complete spreading of water on the entire.

In conclusion, It is clear that nanotube formed on the femtosecond laser textured Ti-35Nb-xHf alloys have arrays of nano/micro structure. Therefore, surface morphology of nano/micro structure will enhance osseointegration and cell adhesion. Also, That can applicate for biomaterials, because hybrid surface has micro/nano structure with non-toxicity, wider surface area, and high corrosion resistance.

- Reference -

1. K. Das and S. Bose, A. Bandyopadhyay, Acta Biomaterialia. 3 (2007) 573
2. M. Long, H. J. Rack, Biomaterials. 19 (1998) 1621
3. M. Niinomi, Biomaterials. 24 (2003) 2673
4. W. G. Kim, H. C. Choe, Y. M. Ko, W. A. Brantley, Thin Solid Film. 517 (2009) 5033
5. R. G. Zhang, V.L. Acoff, Mater. Sci. Eng. 463A (2007) 67
6. E. W. Collings, Physical Metallurgy of Titanium Alloys, ASM, Metals Park, OH, (1984)
7. B. D. Boyan, T. W. Hummert, D. D. Dean and Z. Schwartz, Biomaterials. 17 (1996) 137
8. M. Wong, J. Eulenberger, R. Schenk and E. Hunziker, J. Biomed. Mater. Res. 29 (1995) 1567
9. C. Momma, S. Nolte, N. Chichkov, F. W. Alvensleben and A. Tunnermann, Appl. Surf. Sci. 109 (1997) 15
10. Y. T Sul, CB Johansson, S Petronis, A. Krozer, Y Jeong, A Wennerberg. Biomaterials. 23 (2002) 491
11. B.C Yang, M Uchida, H.M Kim, X.D Zhang, T Kokubo, Biomaterials. 25 (2004) 1003.
12. Y. H Jeong, K. Lee, H. C Choe, Y. M Ko, W. A. Brantley, Thin Solid Films. 517 (2009) 5365
13. D. M. Brunette, P. Tengvall, M. Textor, P. Thomsen, Titanium in Medicine, Springer. (2001) 25
14. Y. Okazaki, Y. Ito, K. Kyo, T. Tateisi, Mater Sci Eng. A213 (1996) 138
15. S. Winter, D. Velten, F. Aubertin, Metallic Biometerial Interfaces, Willy-VCH, (2008) 5.
16. J. Y. Choi, J. G. Kim, B. S. Shin, K. H. W, Journal of the Optical Society of Korea, 7 (2003) 160

17. C. A. Grimes, G. K. Mor, TiO2 nanotube arrays, (2009)
18. J. M. Mack, H. Tsuchiya, A. Ghicov, K. Yasuda, R. Hahn, S. Bauer, P. Schmuki, Current Opinion in Solid State and Materials Science, 11 (2007) 3
19. H. Chen, X. Chen, Y. Zhang, Y. Xia, Laser Physics. 17 (2007) 1378
20. H. C. Choe, W. G. Kim, Y. H. Jung, Surface & Coating Technology 205 (2010) s305
21. W. G. Kim, H. C. Choe, Y. M. Ko, W. A. Brantley, Thinsolid Films, 517 (2009) 5033
22. D. A. Puleo, A. Nanci, Biomater. 20 (1999) 2311.
23. C. Y. Liang, X. J. Yang, Q. Wei, Z. D. Cui, App. Surf. Sci. 255 (2008) 515
24. G. Mendonca, D. B. S. Mendonca, F. J. L. Aragao, L. F. Cooper, Biomater. 29 (2008) 3822
25. J. U Kim, B. H. Kim, K. Lee, H. C. Choe, Y. M Ko, J. Nanosci Nanotech, doi:10.1166/jnn.2011., 3418
26. K. Yasuda, J. M Macak, S. Berger, A. Ghicov, P. Schmuki, Journal of Electrochemical Society, 154 (2007) C472
27. J. H. Zhou, J. P. He, G. W. Zhao, C. H. Zhang, J. S. Zhao, H. P. Hu, Trans. Nonferrous Met. SOC. China. 17 (2007) 82
28. K. Yasuda, P. Schmuki, Electrochimica Acta 52 (2007) 4053
29. H. C. Choe, Y. M. Ko, W.A. Brantley, NSTI-Nanotech 2. (2007) 744
30. J. M. Macak, H. T Suchiya, A. Ghicov, K. Yasuda, R. Hahn, S. Bauer, et al. Curr. Opin Solid State Mater Sci. 11 (2007) 3
31. Y. H. Jeong, K. Lee, H. C. Choe, Y. M. Ko and W. A. Brantley, Thin solid Films. 517 (2009) 5365
32. V. S. Saji, H. C. Choe, W. A. Brantely, Acta Biomater. 5 (2009) 2303
33. S. Oh, C. Daraio, L. H. Chen, T. R. Pisanic, R. R. Finones, S. Jin, J. Biomed. Mater. Res. A 78 (2006) 97
34. M. Uchida, H. M. Kim, T. Kokubo, S. Fujibayshi, T. Nakamura, J.

Biomed. Mater. Res. 64 (2003) 164

35. D. Q. Martins, W. R. Osorio, M. E. P. Souza, R. Caram, A. Garcia, Electrochimica Acta. 53 (2008) 2809

36. K. Yasuda, P. Schmuki, Adv. Mater. 19 (2007) 1757

감사의 글

어려운 영어논문 한편과 시작한 대학원생활이 어느덧 종점을 향하며 졸업논문의 마무리를 글로 남기려니 감회가 새롭습니다. 그동안 연구실에서 함께 동고동락하며 지낸 시간들이 소중한 추억으로 남아 머릿속을 스쳐 지나갑니다.
나의 인생에 또 한 번의 어려운 과정을 값지게 마칠 수 있도록 도움을 주신 분들께 짧게나마 감사의 마음을 전합니다.

우선 참으로 부족한 저를 항상 다독여 주시며 아낌없는 격려와 지도로 큰 가르침을 주신 평생스승인 지도교수 최한철 교수님의 은혜에 고개 숙여 감사드립니다. 가끔씩 뵙지만 언제나 따뜻한 미소로 반겨주시며 격려해주신 재료학교실의 버팀목 고영무 교수님, 바쁘신 가운데 여러모로 챙겨주시고 열과 성으로 심사해 주신 김병훈 교수님께 큰 감사의 뜻을 전합니다. 교수님들 항상 건강하십시오.

낯선 미국 땅에서 새롭게 시작하는 용훈이 형 열심히 하셔서 꼭 금의환향하세요. 항상 끊임없는 조언과 나의 부족한 부분을 채워주시려 노력했던 강이 형 항상 감사히 생각하고 있습니다. 올해는 꼭 좋은 분 만나셔서 저 좀 괴롭히지 마세요. 나의 동기 윤엽아 어디서 머하니 돌아오렴, 보고 싶구나. 신혼의 단꿈에 흠뻑 빠져있는 동엽아 행복하게 잘~살아라. 나의 동창 병학이 매사에 성실하게 임하는 너와 함께 대학원생활 해서 기뻤다. 뭐든 시키면 쫌만 인상 쓰며 말 잘 듣는 착한 은주, 예의바른 사나이 심재원, 앞으로 대학원에 올 영진이, 많은 조언을 해준 승현이, 원기 형, 영현 씨, 영선 씨 모두 모두 감사합니다.
여러분의 앞날에 무한한 영광과 발전이 함께 하시길 바랍니다.

지각하지 않게 하루도 빼놓지 않고 모닝콜해준 혜원,
그리고 우리 사랑하는 가족들,
큰누나 둘째누나 막내누나 항상 고마워~
아들 잘되라고 고생 하신 부모님 대학원 보내주시고 항상 묵묵히 응원해 주셔서 감사합니다. 건강하게 오래 오래 사세요. 자랑스러운 아들이 되도록 더욱 노력하는 모습 보여드리겠습니다.

글로나마 감사의 마음을 표현 할 수 있어서 다행이라 생각하며 다시 한 번 모든 분들께 고개숙여 감사드립니다.

저작물 이용 허락서

학 과	치의생명공학	학 번	20097368	과 정	석사
성 명	한글: 김 재 운 한문 : 金 在 雲 영문 : Kim Jae-Un				
주 소	전남 담양군 남면 경상리 281				
연락처	E-MAIL : whstar7@hanmail.net				
논문제목	한글 : 생체재료용 펨토초레이저 처리한 Ti-35Nb-xHf 합금의 나노튜브 표면 형상 영어 : Nanotubular Surface Morphology of Femtosecond laser Treated Ti-35Nb-xHf Alloys for Biomaterials				

본인이 저작한 위의 저작물에 대하여 다음과 같은 조건아래 조선대학교가 저작물을 이용할 수 있도록 허락하고 동의합니다.

- 다 음 -

1. 저작물의 DB구축 및 인터넷을 포함한 정보통신망에의 공개를 위한 저작물의 복제, 기억장치에의 저장, 전송 등을 허락함
2. 위의 목적을 위하여 필요한 범위 내에서의 편집・형식상의 변경을 허락함. 다만, 저작물의 내용변경은 금지함.
3. 배포・전송된 저작물의 영리적 목적을 위한 복제, 저장, 전송 등은 금지함.
4. 저작물에 대한 이용기간은 5년으로 하고, 기간종료 3개월 이내에 별도의 의사 표시가 없을 경우에는 저작물의 이용기간을 계속 연장함.
5. 해당 저작물의 저작권을 타인에게 양도하거나 또는 출판을 허락을 하였을 경우에는 1개월 이내에 대학에 이를 통보함.
6. 조선대학교는 저작물의 이용허락 이후 해당 저작물로 인하여 발생하는 타인에 의한 권리 침해에 대하여 일체의 법적 책임을 지지 않음
7. 소속대학의 협정기관에 저작물의 제공 및 인터넷 등 정보통신망을 이용한 저작물의 전송・출력을 허락함.

동의여부 : 동의(0) 반대( )

2011 년 02 월 25 일

저작자: 김 재 운 (서명 또는 인)

조선대학교 총장 귀하